

Article

A Comparative Numerical Study of Heat and Mass Transfer Individualities in Casson Stagnation Point Fluid Flow Past a Flat and Cylindrical Surfaces

Khalil Ur Rehman ^{1,2,*}, Wasfi Shatanawi ^{1,3,*}  and Saba Yaseen ²

¹ Department of Mathematics and Sciences, College of Humanities and Sciences, Prince Sultan University, Riyadh 11586, Saudi Arabia

² Department of Mathematics, Air University, PAF Complex E-9, Islamabad 44000, Pakistan

³ Department of Mathematics, Faculty of Science, The Hashemite University, P.O. Box 330127, Zarqa 13133, Jordan

* Correspondence: kurrehman@psu.edu.sa (K.U.R.); wshatanawi@psu.edu.sa (W.S.)

Abstract: There is a consensus among researchers that the simultaneous involvement of heat and mass transfer in fluid flow owns numerous daily life applications like energy systems, automobiles, cooling of electronic devices, power generation by the stream, electric power, and diagnosing and characterizing diseases, to mention just a few. Owing to such motivation, we considered both heat and mass transfer aspects in non-Newtonian fluid flow regimes. The Casson fluid is considered as a non-Newtonian fluid. For better novelty the flow is considered at both flat and cylindrical surfaces along with stagnation point, magnetic field, mixed convection, heat generation, viscous dissipation, thermal radiations, and temperature-dependent thermal conductivity. The ultimate differential equations are nonlinear, and hence difficult to solve analytically. Therefore, a numerical scheme, namely the shooting method with the Runge–Kutta algorithm, is adopted to report an acceptable solution for flow field description. The outcomes are shared comparatively for flat and cylindrical surfaces. We have seen that compared to a flat surface, the cylindrical surface has a larger Nusselt number magnitude.

Keywords: numerical solution; heat transfer; mass transfer; casson fluid; shooting method; Runge–Kutta scheme

MSC: 76R10; 76-10; 65K05



Citation: Rehman, K.U.; Shatanawi, W.; Yaseen, S. A Comparative Numerical Study of Heat and Mass Transfer Individualities in Casson Stagnation Point Fluid Flow Past a Flat and Cylindrical Surfaces.

Mathematics **2023**, *11*, 470. <https://doi.org/10.3390/math11020470>

Academic Editors: Katta Ramesh and Rama Subba Reddy Gorla

Received: 9 November 2022

Revised: 31 December 2022

Accepted: 9 January 2023

Published: 16 January 2023



Copyright: © 2023 by the authors. Licensee MDPI, Basel, Switzerland. This article is an open access article distributed under the terms and conditions of the Creative Commons Attribution (CC BY) license (<https://creativecommons.org/licenses/by/4.0/>).

1. Introduction

The Casson multiphase suspensions are well suited for coating purposes, given the numerous engineering uses of highly thick multiphase flows such as in the chemical and textile industries [1]. As a limiting scenario for the validation, magnetized multiphase flows are also contrasted with the earlier study. Among other cutting-edge uses of this fluid model [2], blood flow in the arteries is a typical illustration of Casson fluid flow [3]. This approach is used to design new medical devices for delivering cells to the nervous system as well as in numerous modified delivery systems. Non-Newtonian fluids are being used in more and more industrial and engineering operations. The Casson fluid model [4] is widely used in biomechanics and the polymer processing industries to describe non-Newtonian fluid dynamics [5]. When a non-Newtonian Casson fluid was used to represent the peristaltic flow of rheologically complicated physiological fluids in a two-dimensional conduit, Mernone et al. [6] took this into consideration. The flow equations were solved using the perturbation series approach. It was discovered that Newtonian fluid was a significant subgroup of non-Newtonian fluids and might serve as an appropriate representation of several physiological processes. Analytical and numerical solutions were

offered. Das and Nandkeolyar [7] offered the solution of time-dependent magnetized Casson fluid across a vertical plate. Using suitable variables, the equations regulating flow transport were converted to the reduced form and then analytically solved using the Laplace transform approach. The numerical values of Sherwood, Nusselt, and skin friction are obtained. The fluid temperature and velocity were observed to decline with rising Casson parameter values. The concentration also shows an opposite trend towards Schmidt number and chemical reaction. A fluid flow model like this has many industrial and medicinal uses, including the creation of glass, paper and the investigation of blood flow. The Falkner–Skan magnetized Casson flow towards the wedge was discussed by Raju and Sandeep [8]. Thermal radiation was linear in most of the investigations that have been done, but in this investigation the thermal radiation was measured nonlinearly. Results were obtained by using the R–K scheme. For three wedge positions, the influence of parameters on the distributions of concentration, temperature, and velocity was explained. They also calculated mass, heat, and friction factor transfer rates for engineering purposes. At various wedge positions it was found that the concentration, temperature, and momentum boundary layers were not uniform. Additionally, it was noted that as the wedge was traveling forward, there was a significant rate of heat and mass transmission. The convective Casson fluid toward the nonlinear surface was discussed by Ahmed et al. [9]. They thought about first-order chemical reactions. The controlling PDEs were transformed into ODEs using similar approaches. The MATLAB function `bvp4c` was used to acquire the temperature, velocity, and concentration profiles numerically, and they were utilized to calculate the entropy generation number.

To study the heat transfer behavior of magnetized Casson fluid with nanoparticles across a wedge, cone, and plate, Ali and Sandeep [10] created a mathematical model. As a base fluid owned with magnetite nanoparticles, water was also carried. The modified non-linear equations were solved using the R–K–Fehlberg-integration method. We discussed how governing parameters affected profiles, namely temperature and velocity. Tables were used to discuss the heat transfer rate and skin friction while looking at the same parameters. Flow over these surfaces is not uniform. Additionally, it was discovered that the flow over a wedge exhibits good heat transfer performance. Soret–Dufour features in Casson fluid flow by heated exponentially surface were elaborated by Zia et al. [11]. The introduction of novel properties of an exponentially space-dependent heat source. The implementation of appropriate variables allowed partial differential frameworks to be transformed into sets of ordinary differential expressions. Analytical solutions were constructed using a homotopy method. Plotting and detailed analysis of the effects of different embedding factors on concentration, temperature and velocity distributions. Additionally, mass and heat transfer rates as well as skin friction coefficients were calculated and explained. The findings illustrate the temperature's distinct properties as they relate to convective and radiation variables. The Soret and Dufour variables oppositely respond to concentration. An asymptotic solution for squeeze viscoplastic Casson flow was developed by Muravleva [12], by employing the asymptotic method previously suggested by Balmforth and Craster (1999) and Frigaard and Ryan (2004). The boundary conditions at the wall for no-slip and slip yield were taken into account. Full slip at the wall (slip) or partial slip at the wall (stick-slip) were both feasible. Utilizing augmented lagrangian methods and accelerated proximal gradient, they verify the numerically obtained solution. Alwawi et al. [13] examined magnetized nanofluid toward the sphere. The nanofluid model developed by Tiwari and Das was used to examine how a magnetic field and nanoparticles affected a naturally occurring convective flow. To resolve the altered system of partial differential equations, the Keller-box method was used. Plotting and analysis were done to determine the effects of parameters on the flow field. The flow field is largely affected by choosing Sodium Alginate-based Casson nanofluid. Divya et al. [14] studied the peristaltic Casson fluid motion via a non-uniform tube while exposed to a radial magnetic field. The channel's wall characteristics were taken into account. Additionally, it was thought that the fluid had changing viscosity, exhibiting exponential change along the channel's width. The

investigations also take into account the Casson fluid's mass and heat transfer properties, using convective boundary conditions and taking into account how thermal conductivity varies with fluid temperature. The model was created to shed light on how blood moves through tiny veins. The perturbation method was used to arrive at the solution to the issue. The graphical analysis shows that the impact of variable viscosity increases on both the size of the bolus created during trapping and the fluid velocity close to the channel walls. Furthermore, due to varying thermal conductivity, temperature of fluid was increased. Liu et al. [15] investigated an unstable stagnation point in Casson fluid. Moreover, the impact of the wall suction and magnetic field on the slide state was considered. Based on these assumptions, a system of nonlinear PDEs was developed and then transformed to dimensionless ODEs. For solution, the MATLAB function `bvp4c` was utilized. For increasing levels of Schmidt number, the fluid concentration and Sherwood number increased and decreased whereas the reverse was seen towards the Thermophoresis parameter. Similarly, the skin friction increases with increasing Casson parameter, suction parameter, and Hartmann number, whereas the rate of heat transfer decreases with increasing Eckert number and increases with increasing thermal radiation and suction. Furthermore, the fluid temperature increased when the Eckert number, Biot number, and heat generation parameter increased.

Azam et al. [16] studied the effects of gyrotactic microorganism in Casson fluid flow with activation energy and bioconvection implications. Additionally, nonlinear radiations and activation energy reverberations were counted. Revisions to a novel nanofluid model were taken into account. Boundary layer theory was used to construct the fundamental PDEs for the chosen research, which were then transformed into nonlinear coupled ODEs using the appropriate transformation. Fehlberg RK45 was used to establish numerical solutions. A comparison assessment was conducted for the purpose of validating the current investigation. The results of this innovative study show that the microorganism density number was abandoned in favor of a more accurate Peclet number, but the enriched Eckert number exhibits the opposite behavior. Additionally, the wall heat flux was negatively impacted by the rising bioconvection Rayleigh number. Kodi and Mopuri [17] investigated the time-dependent Casson fluid flow across an inclined plate with various physical effects. Calculations were done to examine how fluid temperature, velocity, and concentration behaved on an inclined plate when new physical parameters, such as Casson parameter, aligned magnetic field, inclination, and chemical reactions were varied. The tables given for various parameters included the results from Nusselt number, skin friction, and Sherwood number. According to the results of the current analysis, the presence of magnetic field alignment, inclination angle, and Casson fluid parameters sustains a slowing effect on velocity. Venkata et al. [18] addressed the effects of cross diffusion in magnetized Casson fluid flow through a convective surface. The boundary conditions were determined to be convection and diffusive. Using the proper similarity variables, the equations of flow were transformed into a non-dimensional form. The fourth order Runge–Kutta and Shooting methods were used to solve these equations. Plots and tables detailing the effects of various flow factors on the flow fields were provided as results. When Sorret number increased, they noticed that temperature depreciated and concentration increased, while Dufour number admit the opposite effect. The amplification of the non-linear radiative parameter was accompanied by an increase in Sherwood number and a decrease in Nusselt number. Mathematical models for the time dependent flow of Casson fluid with bioconvection and gyrotactic microorganisms were provided by Azam et al. [19]. Additionally, the effects of activation energy and viscous dissipation were taken. To understand flow dynamics in nanomaterials, a redesigned nanofluid model was used. Boundary layer conjecture was used to generate the fundamental PDEs of the assumed research, which were later rearranged into coupled ODEs by using the proper transformation. Using Fehlberg (RK45) shooting, numerical solutions of the considered assessment were obtained. The deprecation of the microorganism density number in favor of a more accurate microorganism difference parameter and Peclet number was noteworthy. The latest improvements on examination of Casson fluid flow can be reached in Ref. [20].

Motivated by the literature reported above, we considered simultaneous aspects of heat and mass transfer in Casson fluid flow towards inclined stretching cylindrical and flat surfaces. The momentum equation is carried in the presence of stagnation point, magnetic field, and mixed convection assumptions, while the energy equation owns viscous dissipation, heat generation, thermal radiations, and temperature dependent-thermal conductivity. It is important to note that to control the turbulence of Casson fluid flow we have considered an externally applied magnetic field. Mathematical flow equations are constructed and solved using the shooting method. The comparative results on flat and cylindrical surfaces are offered by use of tabular data and graphs. We believe that the comparative numerical findings of the present article will be helpful for preceding studies on simultaneous aspects of heat and mass transfer in non-Newtonian fluid flows.

2. Mathematical Formulation

The heat and mass transfer aspects are considered simultaneously in the stagnation point Casson fluid flow regime, subject to inclined flat and cylindrical surfaces. The novelty is increased by considering the magnetic field, heat generation, mixed convection, viscous dissipation, thermal radiations, and variable thermal conductivity. The geometry of the problem is offered in Figure 1. The Casson [21–23] is mathematically modelled as follows:

$$\frac{\partial(\tilde{r}\tilde{u})}{\partial\tilde{x}} + \frac{\partial(\tilde{r}\tilde{v})}{\partial\tilde{r}} = 0, \tag{1}$$

$$\tilde{u}\frac{\partial\tilde{u}}{\partial\tilde{x}} + \tilde{v}\frac{\partial\tilde{u}}{\partial\tilde{r}} = \nu\left(1 + \frac{1}{\beta}\right)\left(\frac{\partial^2\tilde{u}}{\partial\tilde{r}^2} + \frac{1}{\tilde{r}}\frac{\partial\tilde{u}}{\partial\tilde{r}}\right) + \tilde{u}_e\frac{\partial\tilde{u}_e}{\partial\tilde{x}} + g_0B_T(\tilde{T} - \tilde{T}_\infty)\cos(\alpha) + g_0B_C(\tilde{C} - \tilde{C}_\infty)\cos(\alpha) - \frac{\sigma B_0^2}{\rho}(\tilde{u} - \tilde{u}_e), \tag{2}$$

$$\rho c\rho\left(\tilde{u}\frac{\partial\tilde{T}}{\partial\tilde{x}} + \tilde{v}\frac{\partial\tilde{T}}{\partial\tilde{r}}\right) = \frac{1}{\tilde{r}}\frac{\partial}{\partial\tilde{r}}\left(\kappa\frac{\partial\tilde{T}}{\partial\tilde{r}}\right) - \frac{1}{\tilde{r}}\frac{\partial}{\partial\tilde{r}}(\tilde{r}\tilde{q}) + \bar{\mu}\left(1 + \frac{1}{\beta}\right)\left(\frac{\partial\tilde{u}}{\partial\tilde{r}}\right)^2 + Q_0(\tilde{T} - \tilde{T}_\infty). \tag{3}$$

$$\tilde{u}\frac{\partial\tilde{C}}{\partial\tilde{x}} + \tilde{v}\frac{\partial\tilde{C}}{\partial\tilde{r}} = D_m\frac{\partial^2\tilde{C}}{\partial\tilde{r}^2}. \tag{4}$$

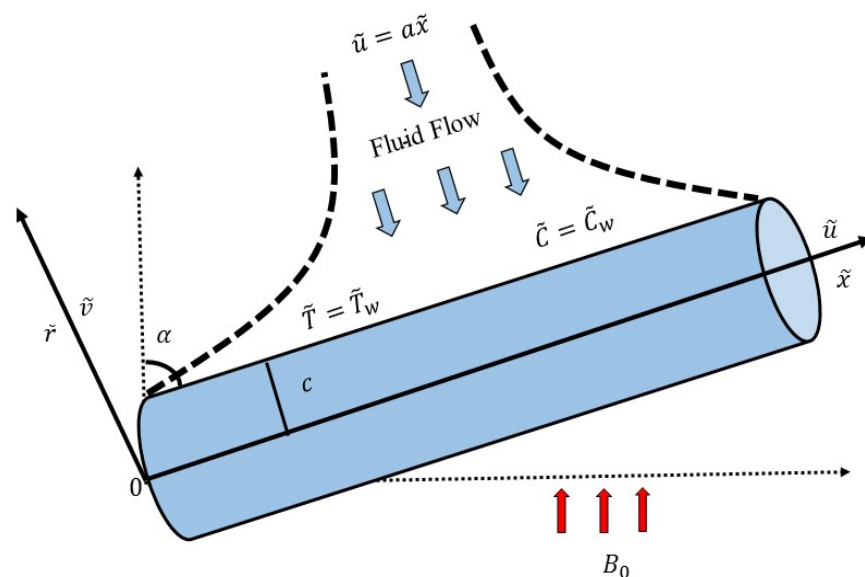


Figure 1. Geometry of the problem.

In the above-mentioned equations there are some parameters, namely, \tilde{v} and \tilde{u} are the fluid velocity components towards \tilde{r} -axis and \tilde{x} -axis, ν is kinematic viscosity, thermal expansion coefficient is denoted by B_T , B_C denotes the coefficient of solutal expansion, acceleration is being produced due to the gravity which is denoted by g_0 , ρ , \tilde{T} , \tilde{C} are

fluid density, temperature and concentration parameters, respectively, D_m represents mass diffusivity, Q_0 is heat generation/absorption coefficient, and radioactive heat flux [24,25] \bar{q} is defined as:

$$\bar{q} = -\frac{\partial \tilde{T}}{\partial \tilde{r}} \frac{16\sigma^* T_\infty^3}{3k^*}. \tag{5}$$

and

$$\kappa(\tilde{T}) = \kappa_\infty \left(1 + \varepsilon \frac{\tilde{T} - \tilde{T}_\infty}{\Delta T} \right), \tag{6}$$

where κ_∞ illustrates that the heat conductivity is far from the surface, and ε is a small parameter. Furthermore:

$$\Delta T = \tilde{T}_w - \tilde{T}_\infty. \tag{7}$$

The conditions given on borderline are:

$$\left. \begin{aligned} \tilde{u}(\tilde{x}, \tilde{r}) &= \tilde{U}_w = a\tilde{x} \\ \tilde{v}(\tilde{x}, \tilde{r}) &= 0 \\ \tilde{T} &= \tilde{T}_w, \tilde{C} = \tilde{C}_w \end{aligned} \right\} \text{ at } \tilde{r} = c, \tag{8}$$

$$\left. \begin{aligned} \tilde{u} &= \tilde{u}_e = d\tilde{x} \\ \tilde{T} &\rightarrow \tilde{T}_\infty, \tilde{C} \rightarrow \tilde{C}_\infty \end{aligned} \right\} \text{ as } \tilde{r} \rightarrow \infty. \tag{9}$$

To get reduced order differential equations we own the following variables:

$$\tilde{u} = \tilde{x} \frac{U_0}{L} f'(\eta), \quad \tilde{v} = -\frac{c}{\tilde{r}} \sqrt{\frac{\nu U_0}{L}} f(\eta) \tag{10}$$

$$\theta(\eta) = \frac{\tilde{T} - \tilde{T}_\infty}{\tilde{T}_w - \tilde{T}_\infty}, \quad \phi(\eta) = \frac{\tilde{C} - \tilde{C}_\infty}{\tilde{C}_w - \tilde{C}_\infty}, \quad \eta = \frac{\tilde{r}^2 - c^2}{2c} \sqrt{\frac{U_0}{\nu L}}.$$

Further, by use of Equation(10), the Equations(2)–(4) turn down to:

$$(1 + 1/\beta)(f'''(1 + 2\gamma\eta) + 2\gamma f'') - f'^2 + ff'' + G_T\theta \cos(\alpha) + G_C\phi \cos(\alpha) \tag{11}$$

$$-M^2(f' - A) + A^2 = 0,$$

$$\left(1 + \frac{4}{3}R \right) (\theta''(1 + 2\eta\gamma) + 2\gamma\theta') + \varepsilon \left((\theta\theta'' + \theta'^2)(1 + 2\eta\gamma) + 2\gamma\theta\theta' \right) \tag{12}$$

$$+PrEc(1 + 2\eta\gamma) \left(1 + \frac{1}{\beta} \right) f''^2 + PrH\theta + Prf\theta' = 0,$$

$$\phi''(1 + 2\eta\gamma) + 2\gamma\phi' + Scf\phi' = 0. \tag{13}$$

The boundary conditions are:

$$f = 0, f' = 1, \phi = 1, \theta = 1, \text{ at } \eta = 0, \tag{14}$$

$$f' = A, \phi = 0, \theta = 0, \text{ as } \eta \rightarrow \infty, \tag{15}$$

were prime indicates the differentiation with respect to η , θ , f , and ϕ are the temperature, velocity and concentration, respectively. The involved parameters are set out as:

$$\begin{aligned} \beta &= \frac{\bar{\mu}\sqrt{2\pi c}}{\tau_r}, R = \frac{4\sigma^* \tilde{T}_\infty^3}{\kappa k^*}, \gamma = \sqrt{\frac{\nu L}{c^2 U_0}}, A = \frac{d}{a}, \\ G_T &= \frac{g_0 \beta_T (\tilde{T}_w - \tilde{T}_\infty) L^2}{U_0 \tilde{x}}, G_C = \frac{g_0 \beta_C (\tilde{C}_w - \tilde{C}_\infty) L^2}{U_0 \tilde{x}}, M = \sqrt{\frac{\sigma B_0^2 L}{\rho U_0}}, Pr = \frac{\bar{\mu} c_p}{\kappa}, \\ Ec &= \frac{U_0^2 (\tilde{x}/L)^2}{c_p (\tilde{T}_w - \tilde{T}_\infty)}, Sc = \frac{\nu}{D_m}, H = \frac{L Q_0}{U_0 \rho c_p}. \end{aligned} \tag{16}$$

Here, Casson fluid and curvature parameters, ratio of free stream to stretching velocity, thermal radiation parameter, thermal Grashof number, the magnetic field parameter Solutal Grashof number, Prandtl number and Eckert number are expressed as $\beta, \gamma, A, R, G_T, M, G_C, Pr$ and Ec , respectively. Further, Sc is Schmidt number. The skin friction coefficient is written as:

$$\left. \begin{aligned} C_f &= \frac{2\tau_w}{\rho U_w^2}, \\ \tau_w &= \bar{\mu} \left(\frac{\partial \tilde{u}}{\partial \tilde{r}} \right)_{\tilde{r}=c'} \\ \sqrt{Re_{\tilde{x}}} C_f &= \left(1 + \frac{1}{\beta} \right) f''(0) \end{aligned} \right\} \tag{17}$$

The Nusselt and Sherwood numbers are expressed as:

$$\left. \begin{aligned} Nu_{\tilde{x}} &= \frac{\tilde{x}q_w}{\kappa(\tilde{T}_w - \tilde{T}_{\infty})}, \\ q_w &= -\kappa \left(1 + \frac{16\sigma^* \tilde{T}_{\infty}^3}{3k^* \kappa} \right) \left(\frac{\partial \tilde{T}}{\partial \tilde{r}} \right)_{\tilde{r}=c'} \\ \frac{Nu_{\tilde{x}}}{\sqrt{Re_{\tilde{x}}}} &= - \left(1 + \frac{4}{3} R \right) \theta'(0) \end{aligned} \right\} \tag{18}$$

$$\left. \begin{aligned} Sh_{\tilde{x}} &= \frac{\tilde{x}J_w}{D_m(\tilde{C}_w - \tilde{C}_{\infty})}, \\ J_w &= -D_m \left(\frac{\partial \tilde{C}}{\partial \tilde{r}} \right)_{\tilde{r}=c'} \\ \frac{Sh_{\tilde{x}}}{\sqrt{Re_{\tilde{x}}}} &= -\phi'(0) \end{aligned} \right\} \tag{19}$$

3. Numerical Scheme

The ODEs are coupled and non-linear, therefore an exact solution in this regard is not possible. Various schemes exist for the solution of fluid flow (see Refs. [25–30]). For a better and more acceptable description of the problem, our intention is to use the shooting method [31] with the R–K scheme. For the implementation of the numerical scheme, we need to drop the order of ODEs by letting:

$$\begin{aligned} y_1 &= f(\eta), y_2 = f'(\eta), y_3 = f''(y_4 = \theta(\eta)), \\ y_5 &= \theta'(\eta), y_6 = \phi(\eta), y_7 = \phi'(\eta), \end{aligned} \tag{20}$$

where prime indicates the differentiation with respect to (η) . When we transform the non-linear coupled ODEs (11)–(13) into system of seven first-order equations that are:

$$y'_1 = y_2, \tag{21}$$

$$y'_2 = y_3, \tag{22}$$

$$y'_3 = \frac{1}{\left(1 + \frac{1}{\beta} \right) (1 + 2\eta\gamma)} \left[\begin{aligned} &-2\gamma y_3 \left(1 + \frac{1}{\beta} \right) + y_2^2 - y_1 y_3 - G_T y_4 \cos \alpha - G_C y_6 \cos \alpha \\ &-M^2(y_2 - A) - A^2 \end{aligned} \right], \tag{23}$$

$$y'_4 = y_5, \tag{24}$$

$$y'_5 = -\frac{1}{\left(1 + \frac{4}{3} R \right) (1 + 2\eta\gamma) + \varepsilon(1 + 2\eta\gamma)y_4} \left[\begin{aligned} &\left(1 + \frac{4}{3} R \right) (2\gamma y_5) + \varepsilon \left((1 + 2\eta\gamma)y_5^2 + 2\gamma y_4 y_5 \right) + \\ &Pr y_1 y_5 + Pr Ec \left(1 + 2\eta\gamma \right) \left(1 + \frac{1}{\beta} \right) y_3^2 + Pr H y_4 \end{aligned} \right], \tag{25}$$

$$y'_6 = y_7, \tag{26}$$

$$y'_7 = \frac{-Sc y_1 y_6 - 2\gamma y_7}{(1 + 2\eta\gamma)}. \tag{27}$$

Now the reduced boundary conditions are:

$$\begin{aligned} y_1 = 0, y_2 = 1, y_4 = 1, y_6 = 1 \text{ at } \eta = 0, \\ y_2 \rightarrow A, y_4 \rightarrow 0, y_6 \rightarrow 0 \text{ as } \eta = \infty. \end{aligned} \quad (28)$$

The above equations are self-coded in Matlab and outcomes are obtained as line graphs and tabular data.

4. Problem Analysis

The investigation is done to explore numerous flow arrangements for the Casson fluid over an inclined surface in the presence of heat and mass transfer aspects. For deep observation, we studied the flow field with and without a magnetic field, heat generation, and thermal radiation effects. After the mathematical modeling we used four final equations to explain the stagnation point flow field, and Equations (1)–(4) represent them. Equations of continuity, momentum, energy and concentration are given as Equations (1)–(3), and (4), respectively. A relation for radioactive heat flux is given as Equation (5), which is represented in terms of the Stefan–Boltzmann constant and mean absorption coefficient. Equation (6) tells us about temperature-dependent thermal conductivity. Equation (7) represents the variation in temperature that correlates with the previous Equation (6). Further, Equations (8) and (9) explain the specific condition at the boundary.

We observe the velocity, temperature, and concentration dispersion at the cylindrical surface with radius ‘ c ’, especially in Equation (8), while Equation (9) contemplates the surface distance from velocity, temperature, and concentration speculation. Our main target is to observe the flow field for plate and cylindrical surfaces. Since we can see the flow Equations (1)–(4) show non-linear behavior and form a system of PDE with the boundary conditions given in Equations (8) and (9), we cannot get the exact solution. We need to reduce the order of the equations that will break down the set of PDEs into the set of ODEs, which will be easy to handle. For this motive, we need to introduce some appropriate variables that are presented in Equation (10). Equations (11)–(13) give us the ultimate flow equations, and $\beta, \gamma, G_T, G_C, M, A$ are Casson fluid parameter, curvature parameter, temperature Grashof number, concentration Grashof number, magnetic field parameter, and velocities ratio parameter, respectively.

These parameters are majorly influencing fluid flow. Equation (12) shows the energy equation with some parameters affecting it, namely curvature parameter, Ec as Eckert number, thermal radiation parameter as R , heat generation parameter as H , Prandtl number is symbolized as Pr . Equation (13) gives us concentration equation containing curvature parameter and Schmidt number Sc . Equations (14) and (15) represent the reduced boundary condition for Equations (11)–(13). In Equation (16), we have the mathematical relation of each flow parameter. Equation (17) states the mathematical form of the skin friction coefficient; on the other hand, Equation (18) works for the mathematical interpretation of the Nusselt number. In Equation (19) we get the mathematical exercise of the Sherwood number. For deep observation of the impact of the flow parameter of the flow field, we solved Equations (11)–(15) by using the shooting method and Runge–Kutta algorithm. Our key interest is to examine the heat and mass transfer aspects of Casson fluid flow towards both flat and cylindrical surfaces. The observed outcomes are shown in the form of graphs and tables. In this regard, we offered Figures 2–11. In detail, Figures 2–4 show the effects of the Casson fluid parameter, magnetic field parameter, and velocities ratio parameter. Figure 2 represents the sequel of the Casson fluid parameter on fluid velocity. We have seen that the fluid velocity admits the inverse behavior. It gradually declined when we enhanced the value of the Casson fluid parameter. It is noted that such a fall is similar for both situations; either we have considered fluid flow over a plate or cylindrical surface. The relationship between a magnetic field and Casson fluid velocity is shown in Figure 3. It exhibits the opposite behavior; as we boost the magnetic field parameter, the Casson fluid velocity begins to decline. It exhibits the same effects on both plate and cylinder, but for a

given magnitude of the magnetic field the velocity on the cylinder is somewhat less than that on the plate.

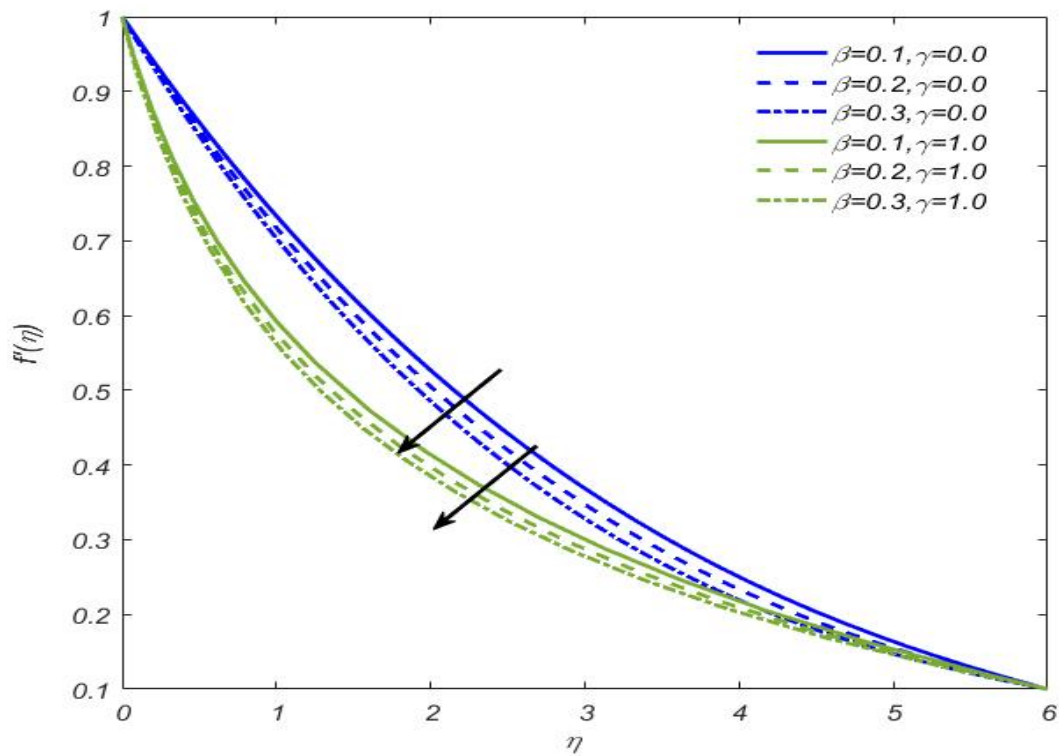


Figure 2. Effect of β on $f'(\eta)$.

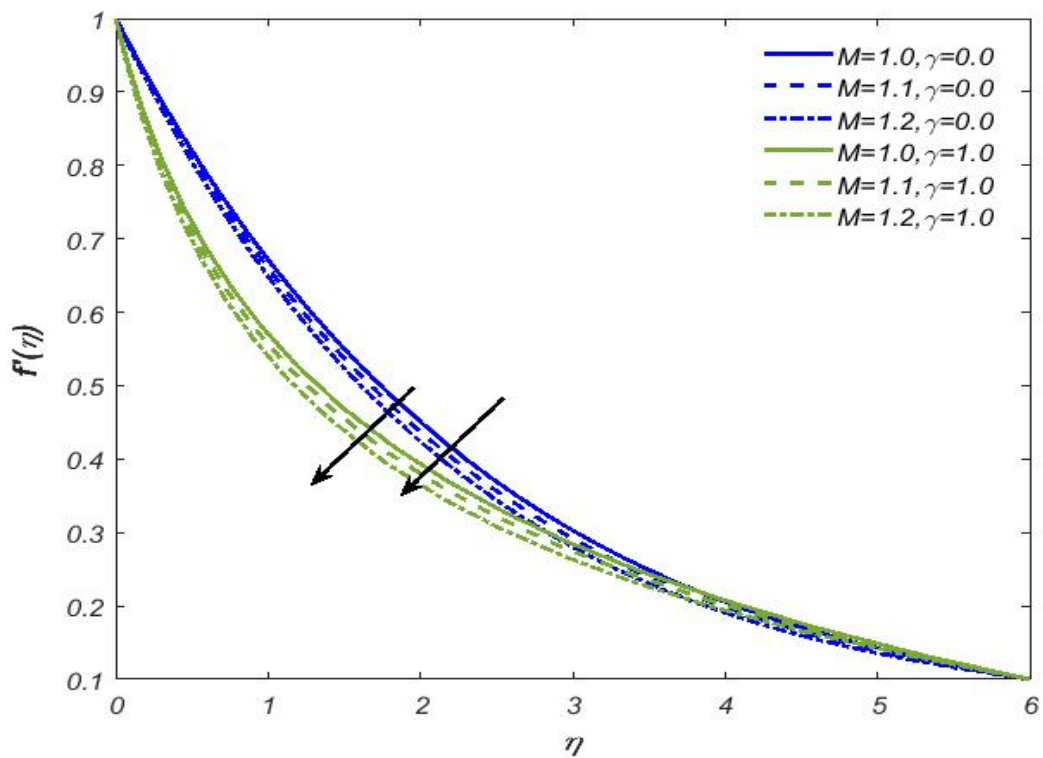


Figure 3. Effect of M on $f'(\eta)$.

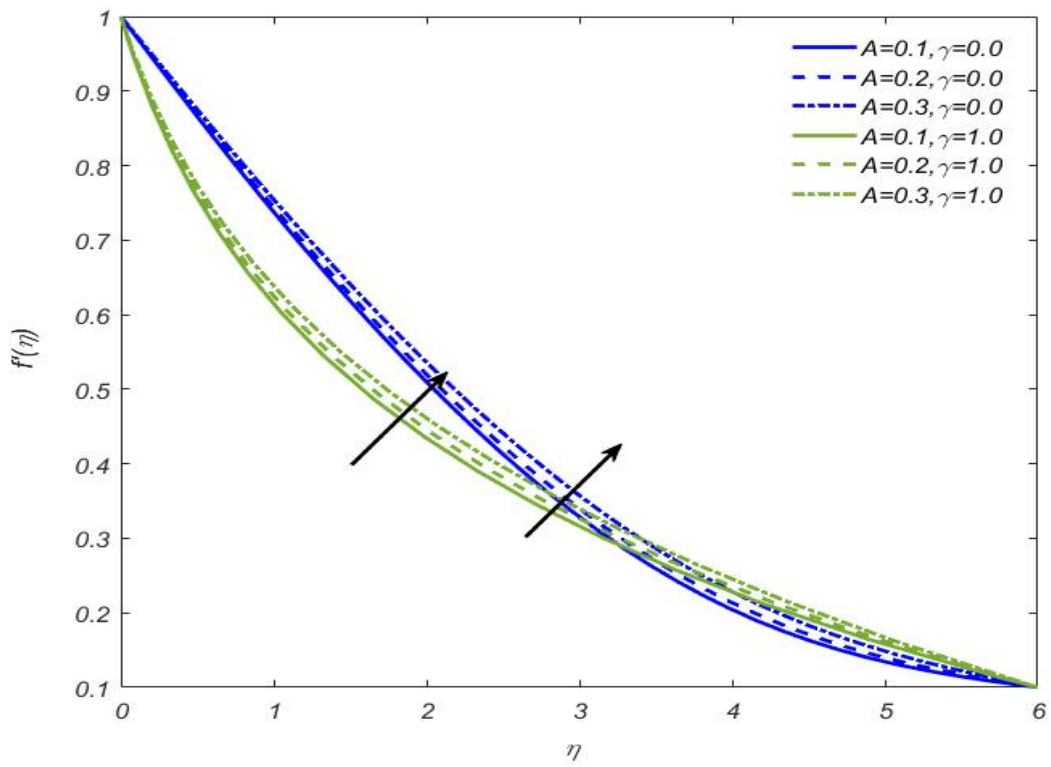


Figure 4. Effect of A on $f'(\eta)$.

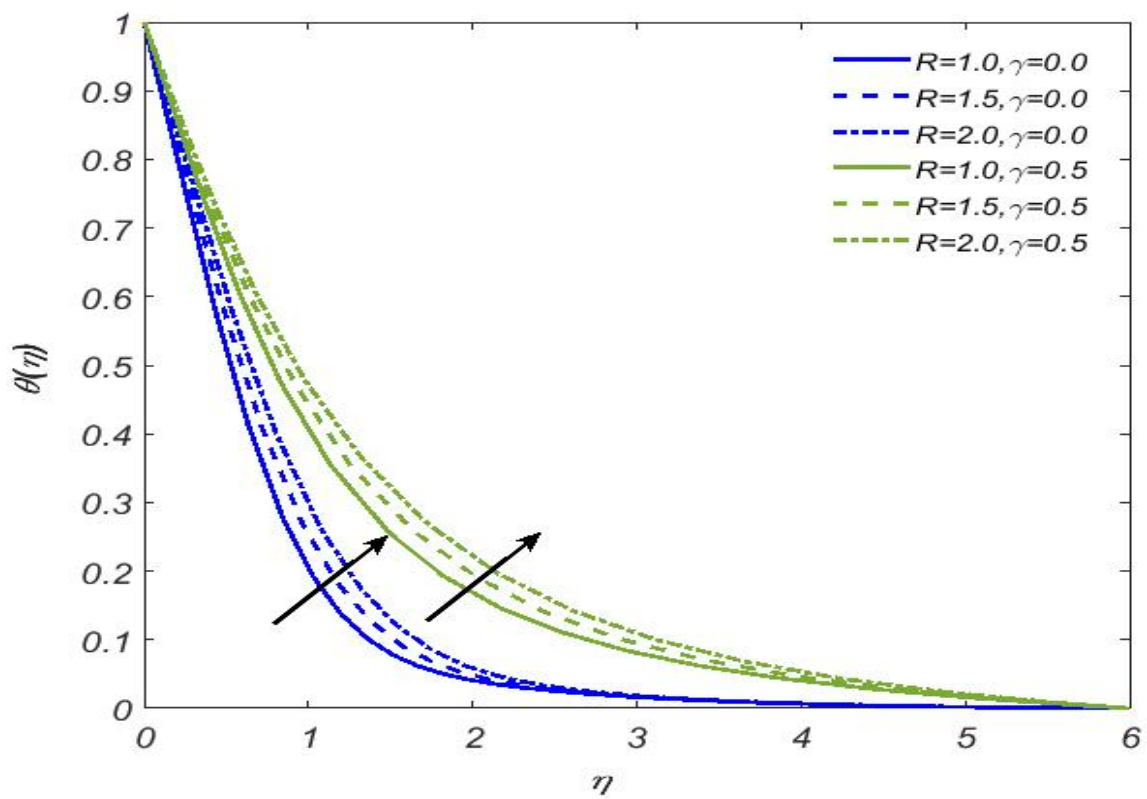


Figure 5. Effect of R on $\theta(\eta)$.

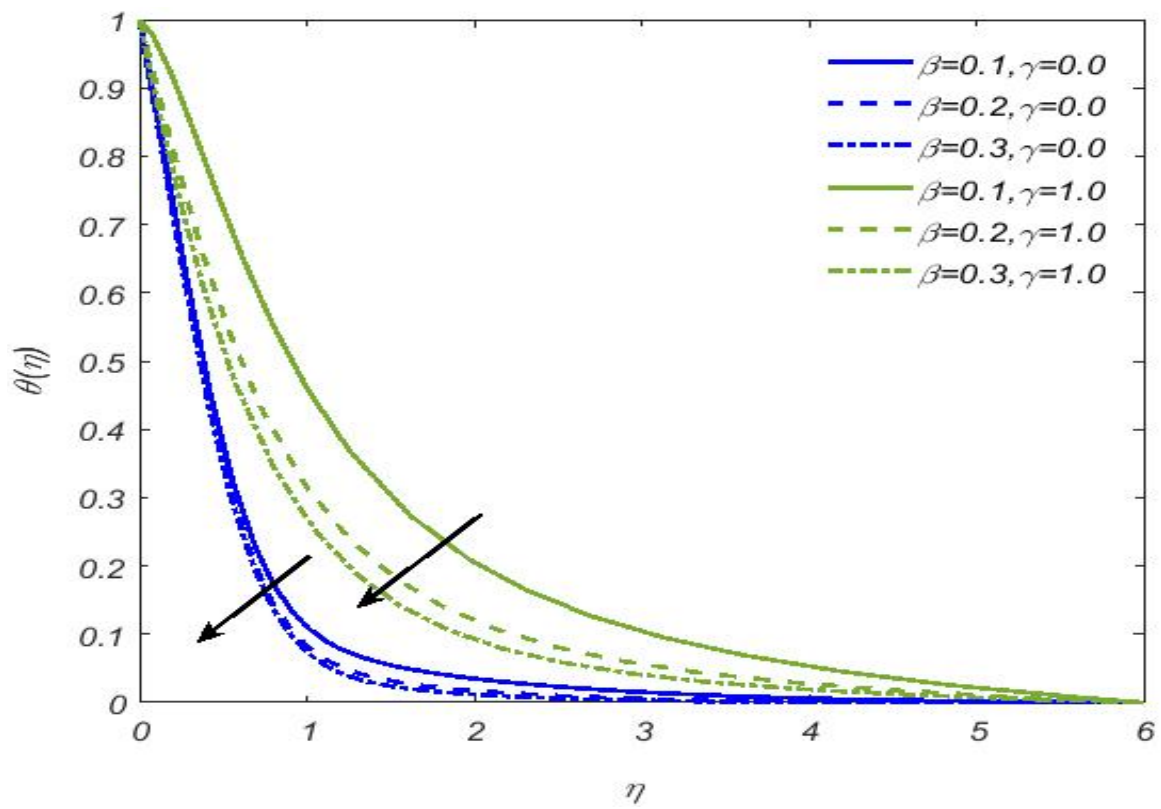


Figure 6. Effect of β on $\theta(\eta)$.

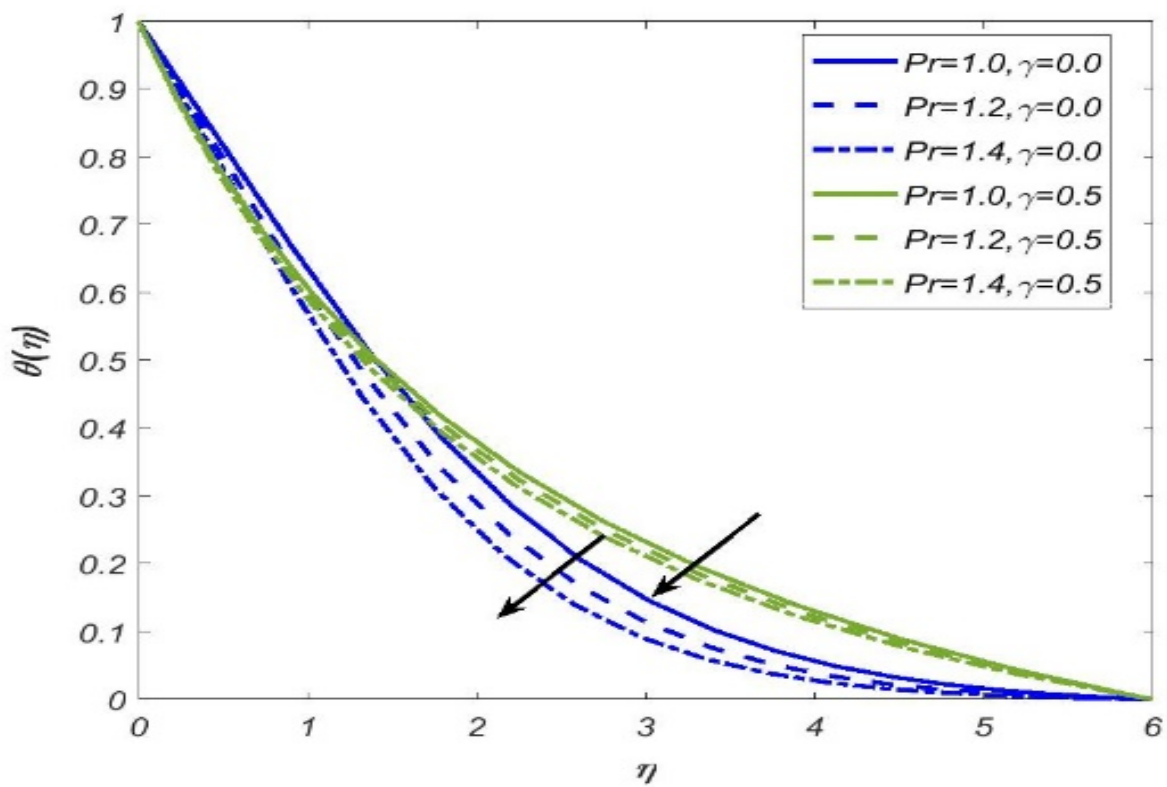


Figure 7. Effect of Pr on $\theta(\eta)$.

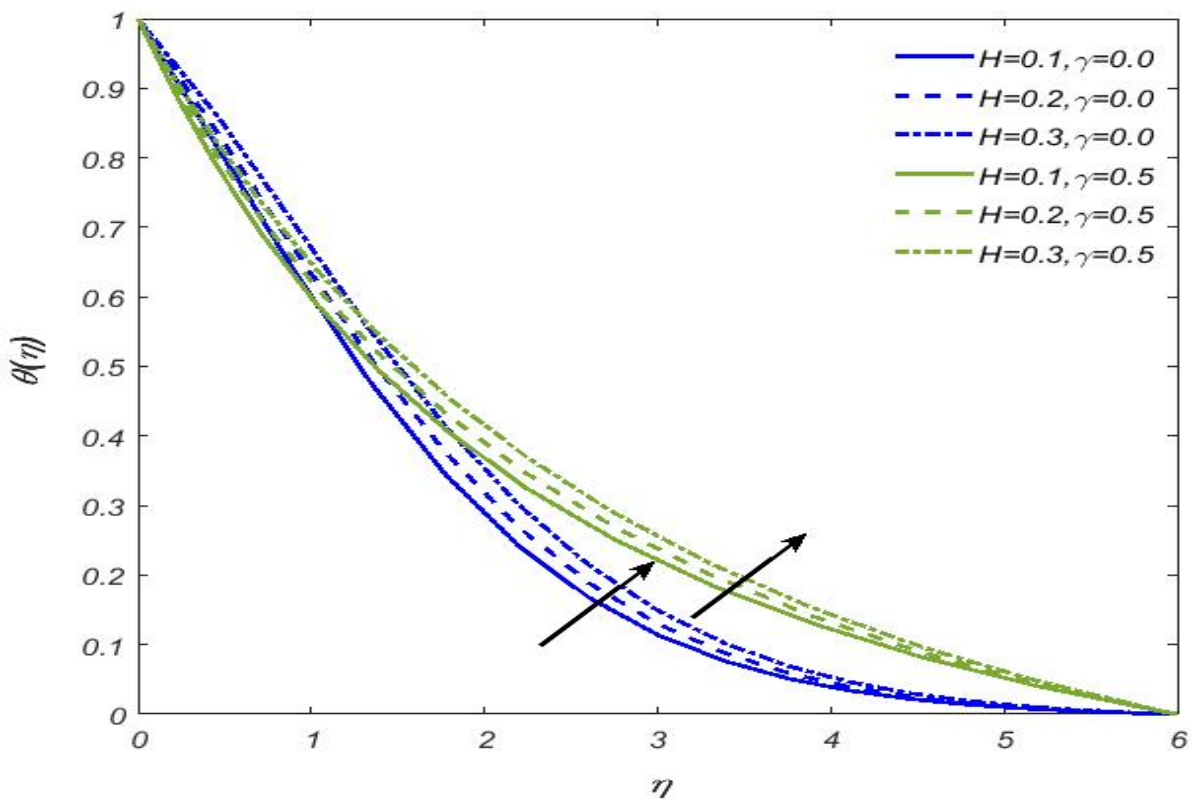


Figure 8. Effect of H on $\theta(\eta)$.

Further, we have seen that the magnitude of the Casson fluid temperature is greater for the cylindrical surface.

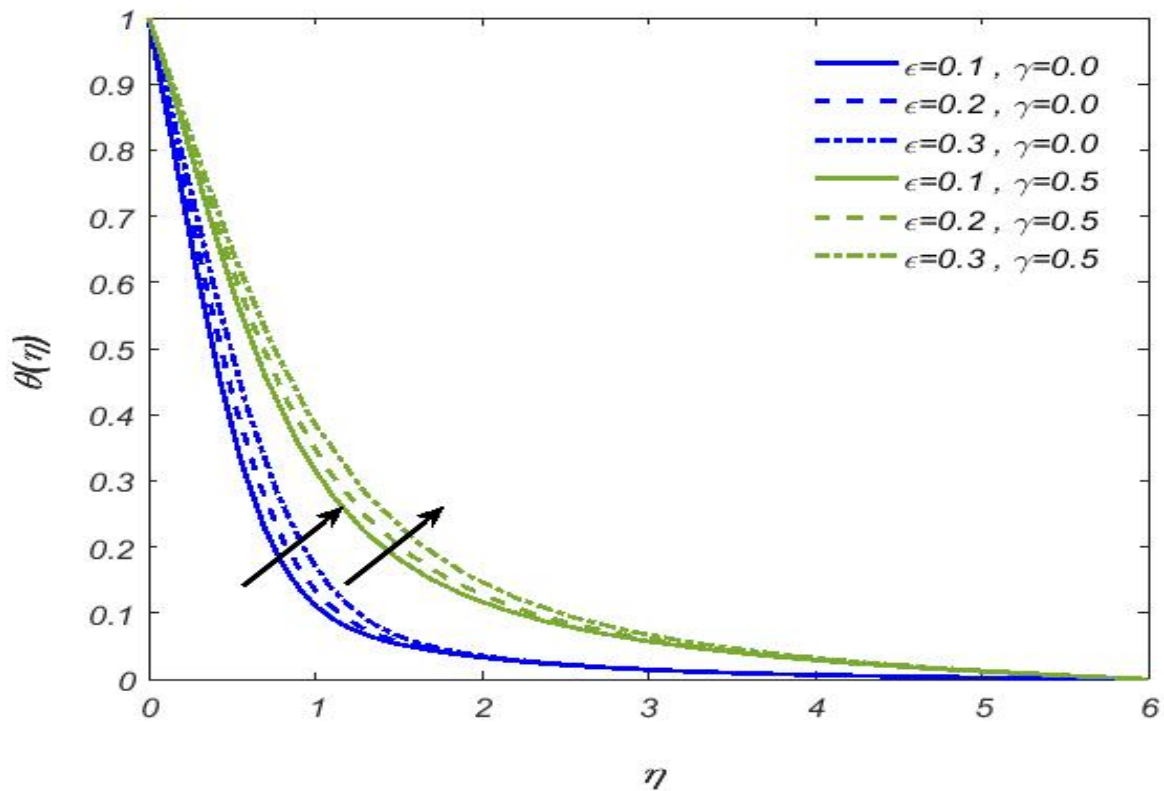


Figure 9. Effect of ϵ on $\theta(\eta)$.

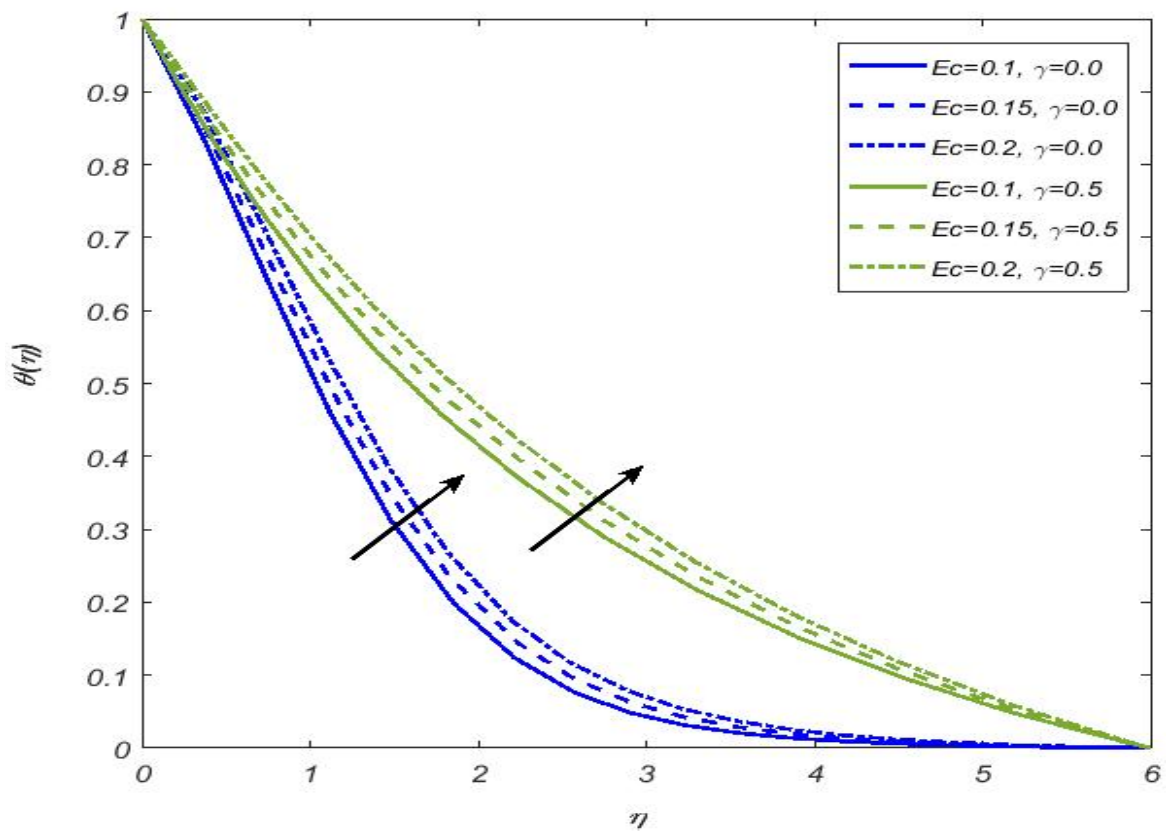


Figure 10. Effect of Ec on $\theta(\eta)$.

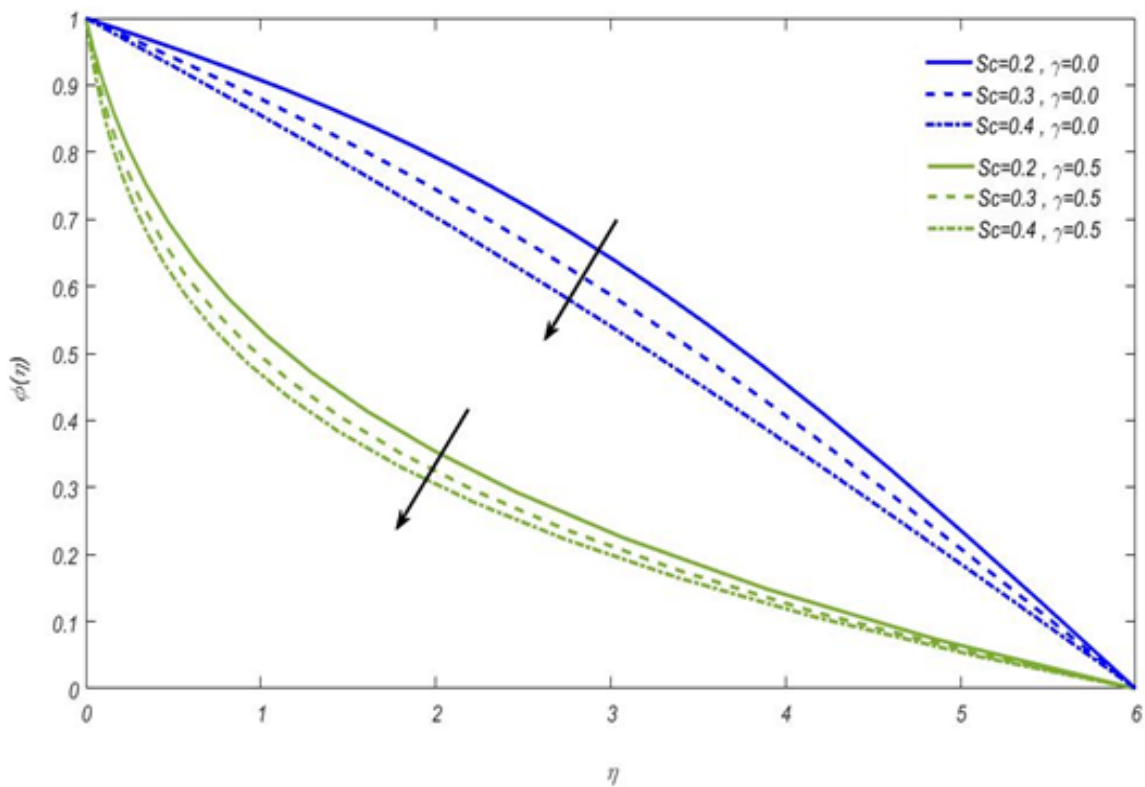


Figure 11. Effect of Sc on $\phi(\eta)$.

Higher values of magnetic field parameter cause increment in Lorentz force, and hence resistance encountered by fluid particles increases. This leads to a decline in fluid velocity. Figure 4 illustrates the impact of the velocity's ratio parameter. We have shown that the Casson fluid velocity is directly impacted by the velocity's ratio parameter, with greater values of the parameter leading to bigger magnitudes of fluid velocity. This impact is the same for both flat and cylindrical surfaces. It is important to note that the velocity ratio parameter shows the ratio of the free stream to the stretching velocity of Casson fluid. When the ratio parameter has a value lower than one, it is inferred that the role of the free stream is less important than the stretching velocity. As a result, the inclined surfaces are causing considerable disturbance in fluid flow. The impact of thermal radiation, Casson fluid, heat generation, variable thermal conductivity parameters, Prandtl and Eckert numbers on Casson fluid temperature is observed. Figures 5–10 are plotted in this direction. In detail, the effect of a thermal radiation parameter on Casson fluid temperature is shown in Figure 5. As the thermal radiation parameter increases the temperature begins to rise, and we can see that both a plate and a cylinder admit a similar effect. The strength of the Casson temperature at the cylinder is higher than the plate. Greater values of radiation parameter produce thermal energy, and hence temperature increases. Figure 6 shows the relation between Casson fluid parameter on the fluid temperature. In contrast to its impact on Casson fluid velocity, it displays an inverse relationship. We have seen that the Casson fluid temperature decreases as the Casson fluid parameter increases. The impact is similar for both plate and cylindrical surfaces. Figure 7 shows the impact of the Prandtl number on the temperature of the Casson fluid. It has the same impact that the Casson fluid parameter does.

The Prandtl number admits an inverse relation towards thermal conductivity and hence the higher values of the Prandtl number cause decline in thermal conductivity as a result the temperature drops.

Under the observation of the same quantity of heat generation and thermal radiation parameter, we have seen the same impact for both plate and cylinder when we increase the value for the Prandtl number the thermal conductivity decrease. This leads to a decline in fluid temperature. Figure 8 shows the impact of the heat generation parameter on the temperature of the Casson fluid. It provides a direct correlation between temperature and the value of the heat generation parameter. This effect is seen for both the plate and the cylinder; however, at some locations, the temperature on the plate is somewhat lower than the temperature on the cylinder. The temperature rises because of energy production brought on by higher values of the heat-generating parameter. Figure 9 shows an increasing effect of variable thermal conductivity on the temperature of the Casson fluid. The temperature of the cylinder and plate progressively rises as we increase the value of the variable thermal conductivity parameter. Such observation holds for both the flat plate and cylindrical surface. Figure 10 shows the effect of the Eckert number on the temperature of Casson fluid for both the plate and the cylinder. After viewing the graph, it is clear that the temperature is rising as we increase the Eckert number under both circumstances. When compared to a flat plate, the temperature magnitude for fluid over a cylindrical surface is larger.

Figure 11 offers the simulation for both cylindrical and flat surfaces. We have seen that for higher values of the Schmidt number the concentration profile admits a declining nature. Such impact is similar for both cylindrical and flat surfaces. We have considered heat and mass transfer aspects, and hence three different physical quantities at the surface are considered to evaluate, namely skin friction coefficient, Nusselt number, and Sherwood number.

They are estimated at both flat surface and cylindrical surfaces. Tables 1–11 are provided in this direction. In detail, for evaluation of the skin friction coefficient (SFC) we considered the following flow parameters, namely solutal Grashof number, and thermal Grashof number. Tables 1–4 are offered in this direction. It is important to note that for evaluation at plate we choose $\gamma = 0$ and for the cylinder we own $\gamma = 0.5$. The effect of the

thermal Grashof number on SFC is given in Table 1 for both scenarios. When we increase the temperature Grashof number, the value of skin friction (in an absolute sense) begins to decrease for both plate and cylinder in the presence of the magnetic field. Further, we have seen that the magnitude of skin friction is higher in the case of Casson fluid past a cylindrical surface. Table 2 demonstrates the impact of the temperature Grashof number on SFC in the absence of a magnetic field. Such observation is done for both the plate and cylinder. It is seen that for higher values of the Grashof number, the skin friction coefficient declines. The strength of skin friction is higher in the case of a cylinder. Further, the values of skin friction coefficient towards temperature Grashof number are higher for the magnetized Casson fluid flow. Such impact holds for both the plate and cylinder. Table 3 determines the values of SFC for positive values of concentration Grashof number. Such observation is done for both flat and cylindrical surfaces. It is noticed that for higher values of concentration Grashof number the skin friction coefficient decreases significantly. The magnitude of SFC is higher for the cylindrical surfaces. Table 4 offers the values of SFC for positive values of concentration Grashof number in the absence of an applied magnetic field. For both cylinder and plate, the skin friction shows decline values towards positive values of concentration Grashof number. The Nusselt number at cylindrical and flat surfaces is evaluated towards various flow parameters which include thermal radiation parameter and Casson fluid parameter, see Tables 5–8. In detail, Table 5 offers how the Nusselt number is affected by the thermal radiation parameter for the plate and cylinder.

Table 1. Impact of G_T parameter on skin friction coefficient.

G_T	$f''(0)$		$(1 + \frac{1}{\beta})f''(0), \beta = 0.1$	
	$\gamma = 0$ (Plate)	$\gamma = 0.5$ (Cylinder)	$\gamma = 0$ (Plate)	$\gamma = 0.5$ (Cylinder)
0.1	−0.2998	−0.5554	−3.2978	−6.1094
0.2	−0.2949	−0.5488	−3.2439	−6.0368
0.3	−0.2899	−0.5423	−3.1889	−5.9653
0.4	−0.2850	−0.5357	−3.1350	−5.8927
0.5	−0.2801	−0.5292	−3.0811	−5.8212
0.6	−0.2752	−0.5227	−3.0272	−5.7497
0.7	−0.2703	−0.5162	−2.9733	−5.6782
0.8	−0.2654	−0.5097	−2.9194	−5.6067
0.9	−0.2605	−0.5033	−2.8655	−5.5363
1.0	−0.2557	−0.4968	−2.8127	−5.4648

Table 2. Impact of G_T on skin friction parameter when $M = 0$.

G_T	$f''(0)$		$(1 + \frac{1}{\beta})f''(0), \beta = 0.1$	
	$\gamma = 0$ (Plate)	$\gamma = 0.5$ (Cylinder)	$\gamma = 0$ (Plate)	$\gamma = 0.5$ (Cylinder)
0.1	−0.2695	−0.5429	−2.9645	−5.9719
0.2	−0.2617	−0.5335	−2.8787	−5.8685
0.3	−0.2539	−0.5252	−2.7929	−5.7772
0.4	−0.2462	−0.5170	−2.7082	−5.6870
0.5	−0.2385	−0.5087	−2.6235	−5.5957
0.6	−0.2308	−0.5004	−2.5388	−5.5044
0.7	−0.2231	−0.4922	−2.4541	−5.4142
0.8	−0.2155	−0.4840	−2.3705	−5.3240
0.9	−0.2078	−0.4758	−2.2858	−5.2338
1.0	−0.2002	−0.4676	−2.2022	−5.1436

Table 3. Impact of G_C parameter on skin friction coefficient.

G_C	$f''(0)$		$(1 + \frac{1}{\beta})f''(0)\beta = 0.1$	
	$\gamma = 0$ (Plate)	$\gamma = 0.5$ (Cylinder)	$\gamma = 0$ (Plate)	$\gamma = 0.5$ (Cylinder)
0.1	-0.2724	-0.5423	-2.9964	-5.9653
0.2	-0.2625	-0.5319	-2.8875	-5.8509
0.3	-0.2552	-0.5215	-2.8072	-5.7365
0.4	-0.2514	-0.5110	-2.7654	-5.6210
0.5	-0.2475	-0.5006	-2.7225	-5.5066
0.6	-0.2434	-0.4901	-2.6774	-5.3911
0.7	-0.2391	-0.4979	-2.6301	-5.4769
0.8	-0.2301	-0.4692	-2.5311	-5.1612
0.9	-0.2199	-0.4588	-2.4189	-5.0468
1.0	-0.2080	-0.4483	-2.2880	-4.9313

Table 4. Impact of G_C on skin friction parameter when $M = 0$.

G_C	$f''(0)$		$(1 + \frac{1}{\beta})f''(0), \beta = 0.1$	
	$\gamma = 0$ (Plate)	$\gamma = 0.5$ (Cylinder)	$\gamma = 0$ (Plate)	$\gamma = 0.5$ (Cylinder)
0.1	-0.2695	-0.5419	-2.9645	-5.9609
0.2	-0.2625	-0.5315	-2.8875	-5.8465
0.3	-0.2551	-0.5210	-2.8061	-5.731
0.4	-0.2473	-0.5106	-2.7203	-5.6166
0.5	-0.2390	-0.5001	-2.629	-5.5011
0.6	-0.2299	-0.4897	-2.5289	-5.3867
0.7	-0.2197	-0.4792	-2.4167	-5.2712
0.8	-0.2077	-0.4688	-2.2847	-5.1568
0.9	-0.1993	-0.4583	-2.1923	-5.0413
1.0	-0.1863	-0.4478	-2.0493	-4.9258

Table 5. Effect of R on Nusselt number.

R	$\theta'(0)$		$-(1 + \frac{4}{3}R)\theta'(0)$	
	$\gamma = 0$ (Plate)	$\gamma = 0.5$ (Cylinder)	$\gamma = 0$ (Plate)	$\gamma = 0.5$ (Cylinder)
0.1	-0.4278	-0.5235	0.4848	0.5933
0.2	-0.4058	-0.5215	0.5140	0.6605
0.3	-0.3868	-0.5200	0.5415	0.7280
0.4	-0.3703	-0.5188	0.5678	0.7954
0.5	-0.3557	-0.5179	0.5929	0.8631
0.6	-0.3428	-0.5171	0.6170	0.9308
0.7	-0.3314	-0.5166	0.6407	0.9988
0.8	-0.3212	-0.5161	0.6638	1.0667
0.9	-0.3121	-0.5157	0.6867	1.1345
1.0	-0.3038	-0.5154	0.7089	1.2026

Table 6. Effect of R on Nusselt number when $H = 0$.

R	$\theta'(0)$		$-(1 + \frac{4}{3}R)\theta'(0)$	
	$\gamma = 0$ (Plate)	$\gamma = 0.5$ (Cylinder)	$\gamma = 0$ (Plate)	$\gamma = 0.5$ (Cylinder)
0.1	-1.4994	-0.9564	1.6993	1.0839
0.2	-1.4302	-0.9383	1.8116	1.1885
0.3	-1.3699	-0.9213	1.9179	1.2898
0.4	-1.3167	-0.9054	2.0189	1.3883
0.5	-1.2693	-0.8905	2.1155	1.4842
0.6	-1.2267	-0.8765	2.2081	1.5777
0.7	-1.1882	-0.8633	2.2972	1.669
0.8	-1.1530	-0.8509	2.3829	1.7585
0.9	-1.1208	-0.8392	2.4658	1.8462
1.0	-1.0912	-0.8281	2.5461	1.9322

Table 7. Impact of β Nusselt number.

β	$\theta'(0)$		$-(1 + \frac{4}{3}R)\theta'(0)R = 0.3$	
	$\gamma = 0$ (Plate)	$\gamma = 0.5$ (Cylinder)	$\gamma = 0$ (Plate)	$\gamma = 0.5$ (Cylinder)
0.1	-0.4052	-0.6093	0.5673	0.8530
0.2	-0.3953	-0.6095	0.5534	0.8533
0.3	-0.3911	-0.6089	0.5475	0.8525
0.4	-0.3888	-0.6085	0.5443	0.8519
0.5	-0.3863	-0.6082	0.5408	0.8515
0.6	-0.3855	-0.6080	0.5397	0.8512
0.7	-0.3850	-0.6078	0.5390	0.8509
0.8	-0.3845	-0.6077	0.5383	0.8508
0.9	-0.3840	-0.6076	0.5376	0.8506
1.0	-0.3838	-0.6075	0.5373	0.8505

Table 8. Effect of β on Nusselt number when $H = 0$.

β	$\theta'(0)$		$-(1 + \frac{4}{3}R)\theta'(0)R = 0.3$	
	$\gamma = 0$ (Plate)	$\gamma = 0.5$ (Cylinder)	$\gamma = 0$ (Plate)	$\gamma = 0.5$ (Cylinder)
1.0	-0.2982	-0.2125	0.4175	0.2975
2.0	-0.3281	-0.4017	0.4593	0.5624
3.0	-0.3412	-0.4635	0.4777	0.6489
4.0	-0.3489	-0.4940	0.4885	0.6916
5.0	-0.3534	-0.5120	0.4948	0.7168
6.0	-0.3562	-0.5238	0.4987	0.7333
7.0	-0.3582	-0.5283	0.5015	0.7396
8.0	-0.3592	-0.5384	0.5029	0.7538
9.0	-0.3605	-0.5432	0.5047	0.7605
10	-0.4250	-0.5470	0.5950	0.7658

Table 9. Effect of Sc on Sherwood number for cylinder.

Sc	$\phi'(0)$	$\frac{Sh_x}{\sqrt{Re_x}} = -\phi'(0)$
	$\gamma = 0.5$	$\gamma = 0.5$
0.1	−0.4131	0.4131
0.2	−0.3493	0.3493
0.3	−0.2724	0.2724
0.4	−0.1767	0.1767
0.5	−0.0527	0.0527
0.6	0.1167	−0.1167
0.7	0.2040	−0.2040
0.8	0.7897	−0.7897
1.0	1.7318	−1.7318

Table 10. Effect of Sc on Sherwood number for plate.

Sc	$\phi'(0)$	$\frac{Sh_x}{\sqrt{Re_x}} = -\phi'(0)$
	$\gamma = 0$	$\gamma = 0$
0.3	−0.4543	0.4543
0.4	−0.1782	0.1782
0.45	−0.0365	0.0365
0.5	−0.0301	0.0301
0.55	0.1494	−0.1494
0.6	0.2486	−0.2486
0.7	0.3067	−0.3067
0.8	0.5355	−0.5355
1.0	0.6399	−0.6399

Table 11. Effect of γ on Sherwood number.

γ	$\phi'(0)$	$\frac{Sh_x}{\sqrt{Re_x}} = -\phi'(0)$
0.1	−0.0098	0.0098
0.2	−0.0190	0.0190
0.3	−0.0374	0.0374
0.4	−0.1680	0.1680
0.5	−0.2724	0.2724
0.6	−0.3591	0.3591
0.7	−0.4354	0.4354
0.8	−0.5049	0.5049
0.9	−0.5697	0.5697
1.0	−0.6308	0.6308

The Nusselt number rises in both circumstances as thermal radiation strength rises. Further, the magnitude of the Nusselt number is greater for the case of the cylindrical surface. Table 6 gives the impact of the thermal radiation parameter on the Nusselt number at both plate and cylindrical surfaces, when the heat generation effect is absent.

For both frames, we observed that higher values of radiation parameter result in higher values in the Nusselt number. Important to note that the strength of the Nusselt number is higher in the case of a flat plate. The effect of the Casson fluid parameter on the Nusselt number is evaluated for both plate and cylindrical surfaces.

Table 7 is offered in this regard. We observed that with greater values of the Casson fluid parameter the Nusselt number declines ordinarily. Further, the magnitude of the Nusselt number is slightly higher on a cylindrical surface. Table 8 gives the examination of

Nusselt number at the plate and cylindrical surfaces towards Casson fluid parameter for the absence of heat generation effect.

We observed that the higher values of the Casson fluid parameter cause inclination in the Nusselt number. Further, we have seen that for positive values of the Casson fluid parameter the magnitude of the Nusselt number is higher for cylinders. The Sherwood number is evaluated for both flat and cylindrical surfaces towards different flow variables.

Tables 9–11 are offered in this regard. The effect of the Schmidt number on the Sherwood number is examined at the cylindrical surface (see Table 9). We have seen that for the higher values of Schmidt number, up to $Sc = 0.5$, the Sherwood number declines.

Table 10 offers the impact of the Schmidt number on the Sherwood number for the case of a flat plate. We have seen that for the Schmidt number up to $Sc = 0.5$, the Sherwood number declines. The influence of the curvature parameter on the Sherwood number is observed, as shown in Table 11. We have seen that the positive variation in curvature causes an increment in the Sherwood number. Our research problem was reduced to Hayat et al. [21] in the absence of mass transfer, heat generation/absorption, and an externally applied magnetic field. For comparison, the Nusselt number and skin friction coefficient, two separate surface variables, are taken into consideration. In this direction, Tables 12 and 13 make this clear. We found an excellent match that yields the authentication of the present study.

Table 12. Comparison of skin friction coefficient number with Ref. [21].

β	γ	Ref. [21]	Present Study
1.0	0.1	1.2347	1.2135
1.5	0.1	1.1082	1.1030
2.1	0.1	1.0310	1.0150
2.0	0.0	0.9966	0.9643
2.0	0.1	1.0409	1.0214
2.0	0.2	1.0850	1.0413
2.0	0.1	1.2165	1.2032
2.0	0.1	1.0976	1.0743
2.0	0.1	0.9311	0.9101

Table 13. Comparison of Nusselt number with Ref. [21].

ϵ	β	γ	Ref. [21]	Present Study
0.0	1.0	0.2	0.5276	0.5054
0.0	1.4	0.2	0.5316	0.5203
0.0	1.8	0.2	0.5336	0.5124
0.0	2.0	0.0	0.5442	0.5220
0.0	2.0	0.12	0.5336	0.5213
0.0	2.0	0.19	0.5279	0.5016
0.0	2.0	0.19	0.5739	0.5216
0.2	2.0	0.19	0.5308	0.5124
0.3	2.0	0.19	0.5123	0.5061

5. Conclusions

The heat and mass transfer fluid flow are considered simultaneously towards inclined flat and cylindrical surfaces. The Casson fluid is considered a non-Newtonian fluid model. The flow field is considered with stagnation point flow, mixed convection, magnetic field,

heat generation, viscous dissipation, thermal radiations, and variable thermal conductivity which is temperature dependent. The flow field is translated in terms of coupled differential system and solved using the shooting method with the R–K scheme. The outcomes are outlined as follows:

1. For both cylindrical and flat surfaces, the Casson fluid velocity shows a declining nature towards magnetic and Casson fluid parameters while the opposite is the case for the velocity's ratio parameter;
2. Casson fluid temperature shows decline values for Casson fluid parameter and Prandtl number, while the opposite is a trend for thermal radiation, heat generation, variable thermal conductivity parameters, and Eckert number. The temperature is noticeably higher in the case of a cylindrical surface;
3. For both cylindrical and flat surfaces, the positive values of Schmidt number the Casson fluid concentration admit inverse trends;
4. The SFC shows the opposite trend for both the thermal Grashof number and concentration Grashof number. The magnitude of SFC is higher for the case cylindrical surface in comparison with a flat surface;
5. The Nusselt number admits direct relation for thermal radiation parameter, while the opposite is the case for the Casson parameter. The magnitude of the Nusselt number is higher at the cylindrical surface for positive iteration in Casson fluid parameter.

Author Contributions: Methodology, K.U.R. and Saba Yaseen; Software, S.Y.; Validation, W.S.; Formal analysis, K.U.R.; Data curation, W.S. and S.Y.; Writing—original draft, K.U.R.; Supervision, W.S. All authors have read and agreed to the published version of the manuscript.

Funding: This research received no external funding.

Data Availability Statement: Not applicable.

Acknowledgments: The authors would like to thank Prince Sultan University for their support through the TAS research lab.

Conflicts of Interest: The authors declare no conflict of interest.

Nomenclature

\tilde{x}, \tilde{r}	Cylindrical coordinates
\tilde{u}, \tilde{v}	Velocity components
ν	Kinematic viscosity
β	Casson fluid parameter
B_T	Thermal expansion coefficient
g_0	Gravitational acceleration
α	Angle of inclination
B_C	Solutal expansion coefficient
\tilde{T}_∞	Ambient temperature
\tilde{T}	Temperature of fluid
B_0	Magnetic field constant
\tilde{C}	Concentration of fluid
\tilde{C}_∞	Ambient concentration
\tilde{u}_e	Free stream velocity
σ	Fluid electrical conductivity
c_p	Specific heat at constant pressure
ρ	Fluid density
\bar{q}	Radiative heat flux
κ	Variable thermal conductivity
$\bar{\mu}$	Dynamic viscosity
Q_0	Heat generation/absorption coefficient

L	Characteristic length
ε	Small parameter
c	Radius of cylinder
\tilde{C}_w	Surface concentration
U_0	Reference velocity
\tilde{T}_w	Surface temperature
D_m	Mass diffusivity
$f'(\eta)$	Fluid velocity
$\phi(\eta)$	Fluid concentration
$\theta(\eta)$	Fluid temperature
G_T	Temperature Grashof number
G_C	Concentration Grashof number
Pr	Prandtl number
A	Velocity's ratio parameter
R	Radiation parameter
M	Magnetic field parameter
γ	Curvature parameter
k^*	Coefficient of mean absorption
Ec	Eckert number
Sc	Schmidt number
σ^*	Stefan–Boltzmann constant
H	Heat generation/absorption parameter

References

- Batra, R.; Jena, B. Flow of a Casson fluid in a slightly curved tube. *Int. J. Eng. Sci.* **1991**, *29*, 1245–1258. [[CrossRef](#)]
- Das, B.; Batra, R. Secondary flow of a Casson fluid in a slightly curved tube. *Int. J. Non-linear Mech.* **1993**, *28*, 567–577. [[CrossRef](#)]
- Srivastava, V.; Saxena, M. Two-layered model of Casson fluid flow through stenotic blood vessels: Applications to the cardiovascular system. *J. Biomech.* **1994**, *27*, 921–928. [[CrossRef](#)] [[PubMed](#)]
- Dash, R.K.; Mehta, K.N.; Jayaraman, G. Casson fluid flow in a pipe filled with a homogeneous porous medium. *Int. J. Eng. Sci.* **1996**, *34*, 1145–1156. [[CrossRef](#)]
- Eldabe, N.T.; Saddeek, M.G.; El-Sayed, A.F. Heat transfer of MHD non-Newtonian Casson fluid flow between two rotating cylinders. *Mech. Mech. Eng.* **2001**, *5*, 237–251.
- Mernone, A.; Mazumdar, J.; Lucas, S. A mathematical study of peristaltic transport of a casson fluid. *Math. Comput. Model.* **2002**, *35*, 895–912. [[CrossRef](#)]
- Das, M.; Mahato, R.; Nandkeolyar, R. Newtonian heating effect on unsteady hydromagnetic Casson fluid flow past a flat plate with heat and mass transfer. *Alex. Eng. J.* **2015**, *54*, 871–879. [[CrossRef](#)]
- Raju, C.; Sandeep, N. Nonlinear radiative magnetohydrodynamic Falkner-Skan flow of Casson fluid over a wedge. *Alex. Eng. J.* **2016**, *55*, 2045–2054. [[CrossRef](#)]
- Ahmed, S.E.; Mansour, M.; Mahdy, A.; Mohamed, S.S. Entropy generation due to double diffusive convective flow of Casson fluids over nonlinearity stretching sheets with slip conditions. *Eng. Sci. Technol. Int. J.* **2017**, *20*, 1553–1562. [[CrossRef](#)]
- Ali, M.; Sandeep, N. Cattaneo-Christov model for radiative heat transfer of magnetohydrodynamic Casson-ferrofluid: A numerical study. *Results Phys.* **2017**, *7*, 21–30. [[CrossRef](#)]
- Zia, Q.Z.; Ullah, I.; Waqas, M.; Alsaedi, A.; Hayat, T. Cross diffusion and exponential space dependent heat source impacts in radiated three-dimensional (3D) flow of Casson fluid by heated surface. *Results Phys.* **2018**, *8*, 1275–1282. [[CrossRef](#)]
- Larisa, M. Axisymmetric squeeze flow of a Casson medium. *J. Non-Newton. Fluid Mech.* **2019**, *267*, 35–50.
- Alwawi, F.A.; Alkawasbeh, H.T.; Rashad, A.; Idris, R. MHD natural convection of Sodium Alginate Casson nanofluid over a solid sphere. *Results Phys.* **2019**, *16*, 102818. [[CrossRef](#)]
- Divya, B.; Manjunatha, G.; Rajashekhar, C.; Vaidya, H.; Prasad, K. Analysis of temperature dependent properties of a peristaltic MHD flow in a non-uniform channel: A Casson fluid model. *Ain Shams Eng. J.* **2021**, *12*, 2181–2191. [[CrossRef](#)]
- Liu, J.; Abidi, A.; Khan, M.R.; Rasheed, S.; Allehiyany, F.M.; Mahmoud, E.E.; Galal, A.M. Thermal analysis of a radiative slip flow of an unsteady casson nanofluid toward a stretching surface subject to the convective condition. *J. Mater. Res. Technol.* **2021**, *15*, 468–476. [[CrossRef](#)]
- Azam, M.; Xu, T.; Nayak, M.K.; Khan, W.A.; Khan, M. Gyrotactic microorganisms and viscous dissipation features on radiative Casson nanofluid over a moving cylinder with activation energy. *Waves Random Complex Media* **2022**, 1–23. [[CrossRef](#)]
- Kodi, R.; Mopuri, O. Unsteady MHD oscillatory Casson fluid flow past an inclined vertical porous plate in the presence of chemical reaction with heat absorption and Soret effects. *Heat Transf.* **2021**, *51*, 733–752. [[CrossRef](#)]
- Ramudu, A.C.V.; Kumar, K.A.; Sugunamma, V.; Sandeep, N. Impact of Soret and Dufour on MHD Casson fluid flow past a stretching surface with convective–diffusive conditions. *J. Therm. Anal. Calorim.* **2021**, *147*, 2653–2663. [[CrossRef](#)]

19. Azam, M.; Abbas, N.; Kumar, K.G.; Wali, S. Transient bioconvection and activation energy impacts on Casson nanofluid with gyrotactic microorganisms and nonlinear radiation. *Waves Random Complex Media* **2022**, 1–20. [[CrossRef](#)]
20. Hayat, T.; Khan, S.A.; Momani, S. Finite difference analysis for entropy optimized flow of Casson fluid with thermo diffusion and diffusion-thermo effects. *Int. J. Hydrog. Energy* **2022**, *47*, 8048–8059. [[CrossRef](#)]
21. Hayat, T.; Asad, S.; Alsaedi, A. Flow of variable thermal conductivity fluid due to inclined stretching cylinder with viscous dissipation and thermal radiation. *Appl. Math. Mech.* **2014**, *35*, 717–728. [[CrossRef](#)]
22. Rehman, K.U.; Malik, A.A.; Malik, M.; Sandeep, N.; Saba, N.U. Numerical study of double stratification in Casson fluid flow in the presence of mixed convection and chemical reaction. *Results Phys.* **2017**, *7*, 2997–3006. [[CrossRef](#)]
23. Khan, A.U.; Al-Zubaidi, A.; Munir, S.; Saleem, S.; Duraihem, F.Z. Closed form solutions of cross flows of Casson fluid over a stretching surface. *Chaos Solitons Fractals* **2021**, *149*, 111067. [[CrossRef](#)]
24. Azam, M. Effects of Cattaneo-Christov heat flux and nonlinear thermal radiation on MHD Maxwell nanofluid with Arrhenius activation energy. *Case Stud. Therm. Eng.* **2022**, *34*, 102048. [[CrossRef](#)]
25. Azam, M. Bioconvection and nonlinear thermal extrusion in development of chemically reactive Sutterby nano-material due to gyrotactic microorganisms. *Int. Commun. Heat Mass Transf.* **2021**, *130*, 105820. [[CrossRef](#)]
26. Barnoon, P.; Ashkiyan, M. Magnetic field generation due to the microwaves by an antenna connected to a power supply to destroy damaged tissue in the liver considering heat control. *J. Magn. Magn. Mater.* **2020**, *513*, 167245. [[CrossRef](#)]
27. Nazım, K.; Zontul, H.; Sahin, B. Heat transfer and flow characteristics in a sinusoidally curved con-verging-diverging channel. *Int. J. Therm. Sci.* **2020**, *148*, 106163.
28. Barnoon, P. Numerical assessment of heat transfer and mixing quality of a hybrid nanofluid in a microchannel equipped with a dual mixer. *Int. J. Thermofluids* **2021**, *12*, 100111. [[CrossRef](#)]
29. Nazım, K. Experimental investigation of flow structure and heat transfer characteristics for confined cylinders. *Int. Commun. Heat Mass Transf.* **2022**, *133*, 105959.
30. Monfared, R.H.; Niknejadi, M.; Toghraie, D.; Barnoon, P. Numerical investigation of swirling flow and heat transfer of a nanofluid in a tube with helical ribs using a two-phase model. *J. Therm. Anal. Calorim.* **2021**, *147*, 3403–3416. [[CrossRef](#)]
31. Azam, M.; Mabood, F.; Khan, M. Bioconvection and activation energy dynamisms on radiative sutterby melting nanomaterial with gyrotactic microorganism. *Case Stud. Therm. Eng.* **2021**, *30*, 101749. [[CrossRef](#)]

Disclaimer/Publisher’s Note: The statements, opinions and data contained in all publications are solely those of the individual author(s) and contributor(s) and not of MDPI and/or the editor(s). MDPI and/or the editor(s) disclaim responsibility for any injury to people or property resulting from any ideas, methods, instructions or products referred to in the content.